Editors' Suggestion

Symmetry-enforced Fermi degeneracy in topological semimetal $RhSb_3$

K. Wang,[1] L. Wang,[1] I-L. Liu,[1] F. Boschini,[2,3] M. Zonno,[2,3] M. Michiardi,[2,3,4] E. Rotenberg,[5] A. Bostwick,[5] D. Graf,[6] B. J. Ramshaw,[7,8,9] A. Damascelli,[2,3,9] and J. Paglione[1,9]

[1]*Maryland Quantum Materials Center, Department of Physics, University of Maryland, College Park, Maryland 20742, USA*
[2]*Department of Physics and Astronomy, University of British Columbia, Vancouver, British Columbia, Canada V6T 1Z1*
[3]*Quantum Matter Institute, University of British Columbia, Vancouver, British Columbia, Canada V6T 1Z4*
[4]*Max Planck Institute for Chemical Physics of Solids, Nöthnitzer Straße 40, 01187 Dresden, Germany*
[5]*Advanced Light Source, Lawrence Berkeley National Laboratory, Berkeley, California 94720, USA*
[6]*National High Magnetic Field Laboratory, Florida State University, Tallahassee, Florida 32306-4005, USA*
[7]*Pulsed Field Facility, National High Magnetic Field Laboratory, Los Alamos National Laboratory, Los Alamos, New Mexico 87545, USA*
[8]*Laboratory of Atomic and Solid State Physics, Cornell University, 142 Sciences Drive, Ithaca, New York 14853, USA*
[9]*Canadian Institute for Advanced Research, Toronto, Ontario, Canada M5G 1Z8*

(Received 17 October 2022; revised 13 June 2023; accepted 10 July 2023; published 26 July 2023)

Predictions of a topological electronic structure in the skutterudite TPn_3 family (T=transition metal, Pn = pnictogen) are investigated via magnetoresistance, quantum oscillation, and angle-resolved photoemission experiments on $RhSb_3$, a semimetal with low carrier density. Electronic band structure calculations and symmetry analysis of $RhSb_3$ indicate this material to be a zero-gap semimetal protected by symmetry with inverted valence and conduction bands that touch at the Γ point close to the Fermi level. Transport experiments reveal an unsaturated linear magnetoresistance that approaches a factor of 200 at 60 T magnetic fields and quantum oscillations observable up to 150 K that are consistent with a large Fermi velocity ($\sim 1.3 \times 10^6$ m/s), high carrier mobility [~ 14 $m^2/(V\,s)$], and the existence of a small three-dimensional hole pocket. A very small, sample-dependent effective mass falls to values as low as 0.018(2) of the bare electron mass and scales with the Fermi wave vector. This, together with a nonzero Berry's phase and the location of the Fermi level in the linear region of the valence band, suggests $RhSb_3$ as representative of a material family of topological semimetals with symmetry-enforced Fermi degeneracy at the high-symmetry points.

DOI: 10.1103/PhysRevMaterials.7.074205

I. INTRODUCTION

Following the discovery of topological insulators [1,2], new classes of topological materials such as Dirac semimetals [3], Weyl semimetals [4,5], and nodal semimetals [6,7] have developed considerable interest. In Dirac systems, linearly dispersing valence and conduction bands touch at discrete points of fourfold degeneracy in the Brillouin zone (BZ), giving Dirac nodes protected against gap formation by crystal symmetry. Cd_3As_2 and Na_3Bi were the first theoretically predicted Dirac semimetal candidates [8,9], later confirmed by experiments [10–13]. By breaking either inversion or time-reversal symmetry, a Dirac semimetal can be tuned to a Weyl state where the nondegenerate linear touchings of the bulk bands come in pairs [4,5], confirmed by recent experiments on materials such as the TaAs family (type I) [14,15]. Recent studies have shown the existence of other exotic topological semimetal types, such as type-II Weyl semimetals such as WTe_2 and $MoTe_2$ [16,17], nodal-line or nodal-chain semimetals [6,18,19], and triple fermions or beyond [20–24]. The topologically nontrivial band structure in such materials hosts unusual electronic states and exotic physical properties, including the so-called chiral anomaly phenomena and the associated negative magnetoresistance (MR), nonlocal transport, and quantum anomalous Hall effect [25–32]. Interestingly, most Dirac and Weyl semimetals exhibit high mobilities and extremely large values of MR [25,26,28,30–33]: Carrier mobilities in Cd_3As_2, TaAs, and WTe_2 approach 100 $m^2/(V\,s)$, and MR scales of up to ∼5000 are observed in 9 T fields. Extreme MR is believed to arise from the lifting of the high mobility of the Dirac or Weyl node protected by the (crystal or time-reversal) symmetry or large fluctuations in the mobility due to the disorder effect of the Dirac quasiparticles [25,26]. Large MR is also observed in some other semimetals such as LaSb and the $NbSb_2$ family [34–37] related to the topological band properties [38–43].

Although extensive studies have been reported, topological semimetal families are still rare. Seminal theoretical work by Singh and Pickett [44] on the TPn_3 (T = transition metal, Pn = pnictogen) skutterudites that predated the topological revolution identified the possibility of an unusual quasilinear band dispersion structure in the cubic unfilled skutterudite $CoSb_3$ [45]. $CoSb_3$ is a well-known thermoelectric small-gap semiconductor [44,46], that, while topologically trivial, was predicted to be tunable through a topological quantum critical point via displacement of the Sb sublattices. Such a displacement was proposed to decrease gap size toward a critical point where the gap closes and massless (Dirac or Weyl) bands appear [45,47]. With further displacement, spin-orbit coupling would open a gap between inverted bands, realizing a nontrivial topological state. Similar behavior was also proposed in the theoretical compound $IrBi_3$, where band inversion between Ir-d and Bi-p orbitals was predicted to

occur [48]. In this paper, we report on an exploration of the intermediate member $RhSb_3$ using several experimental methods to identify a class of topological semimetals with symmetry-enforced Fermi degeneracy at the high-symmetry points, that is, enforced semimetals with Fermi degeneracy (ESFDs) [23,24], in this skutterudite series. Together with observations of very large MR and high carrier mobility values, quantum oscillation studies of the effective mass and nontrivial Berry's phase, as well as the angle-resolved photoemission spectroscopy (ARPES) experiments, are consistent with first-principles calculations of the electronic structure indicating that a nontrivial topology is present in this family.

II. METHODS

Single crystals of $RhSb_3$ were synthesized by a high-temperature self-flux method. X-ray diffraction data were taken at room temperature with Cu K_α ($\lambda = 0.154\,18$ nm) radiation in a powder diffractometer. Electrical transport measurements up to 14 T were conducted on polished samples in a commercial cryostat applying the conventional four-wire contact method. High-field MR and Shubnikov–de Haas (SdH) oscillation were measured at the National High Magnetic Field Laboratory (NHMFL) Tallahassee DC Field Facility up to 35 T, using a one-axis rotator in a He-3 cryostat with temperature range ~0.35–70 K, and also at the NHMFL Los Alamos pulsed field facility up to 65 T. All measurements were performed with electrical current flowing along the [100] direction. The magnetic field direction was always kept perpendicular to the current, but rotated from perpendicular to the (100) face ($\theta = 0^\circ$) to a direction along the (100) face ($\theta = 90^\circ$). The longitudinal conductivity σ_{xx} is derived through tensor conversion from the longitudinal resistivity ρ_{xx} and the Hall resistivity ρ_{xy} by $\sigma_{xx} = \frac{\rho_{xx}}{\rho_{xx}^2+\rho_{xy}^2}$. The global fitting and uncertainty analysis for the quantum oscillation in the longitudinal conductivity σ_{xx} for $RhSb_3$ single crystals was performed using a Broyden-Fletcher-Goldfarb-Shanno (BFGS) optimizer and a Markov chain Monte Carlo (MCMC) method to compute the joint distribution of parameter probabilities and to find the global minimum, implemented in the BUMPS code [49].

ARPES measurements were performed at beamline 7.0.2.1 of the Advanced Light Source (ALS) at Lawrence Berkeley National Laboratory. The sample was cleaved and kept at 80 K at a base pressure of 5×10^{-11} Torr. Photoemitted electrons were detected with a Scienta R4000 analyzer, for photon energy ranging from 130 to 170 eV. The energy and the angular resolution were better than 50 meV and 0.2°, respectively.

First-principles electronic structure calculations were performed within the full-potential linearized augmented plane-wave (LAPW) method [50] implemented in the WIEN2K package, without or with spin-orbit coupling (SOC) [51]. The generalized gradient approximation (GGA) of Perdew, Burke, and Ernzerhof [52] (PBE) was used for the exchange-correlation potential. The LAPW sphere radius was set to 2.5 bohrs for all atoms. The converged basis corresponding to $R_{\min}k_{\max} = 7$ with additional local orbital was used, where $R_{\min}$ is the minimum LAPW sphere radius and $k_{\max}$ is the plane-wave cutoff. Lattice parameters were obtained from refinement of the x-ray diffraction pattern obtained from powdered single crystals. In the calculation with spin-orbit coupling, the modified Becke-Johnson (mBJ) exchange potential was combined with the GGA correlation [53]. It can effectively mimic the behavior of the orbital-dependent potential around the band gap and so is expected to obtain the accurate position of states near the band edge and the band order, which are the keys to determine the band inversion and the band topology. For high-symmetry points, the eigenvalues (irreducible representations) of all symmetry operators have been computed from the wave functions for each band using the open-source code VASP2TRACE, referring to the character tables in the Bilbao Crystallographic Server (BCS) [54,55].

III. RESULTS AND DISCUSSION

The TSb_3 system with T = Co, Rh, and Ir crystallizes in the symmorphic unfilled skutterudite structure (space group $Im\bar{3}$) with cubic Bravais lattice as shown in Fig. S1 of the Supplemental Material [56]. Without SOC, for the space group $Im\bar{3}$, the Γ point in the first Brillouin zone has a point group symmetry of T_h. In $CoSb_3$, the highest valence band mainly derived from the p orbitals of Sb is found to form an irreducible representation Γ_1^- of the T_h point group, while the three lowest conduction bands dominated by the d-e_g orbitals of the (Co) transition metal atoms form an irreducible representation Γ_4^+. The $CoSb_3$ band structure is highly symmetric, with a single set of occupied and unoccupied bands touching at the high-symmetry Γ point. Turning on SOC lifts the degeneracy of these states and induces a gap of ~50–120 meV between the valence band with an irreducible representation Γ_5^- and the conduction bands with irreducible representations Γ_5^+ and $\Gamma_6^+ + \Gamma_7^+$, for the $m3$ double point group [44,45,57,70], as shown in Fig. 1(a) [45].

In $RhSb_3$, the stronger SOC in Rh atoms pushes the band Γ_5^- up as shown in Fig. 1(b). The energy difference $\eta = E_{\Gamma_6^+ + \Gamma_7^+} - E_{\Gamma_5^-}$, which indicates the strength of the band inversion as SOC is increased, is shown to become negative [Fig. 1(c)]. This implies that band inversion occurs in $RhSb_3$ at the Γ point. The SOC also lifts a degeneracy and opens an ~20 meV gap between the single band Γ_5^+ and the double-degenerated bands $\Gamma_6^+ + \Gamma_7^+$, in Fig. 1(c). Furthermore, the overlap of the valence band Γ_5^- and the conduction bands Γ_5^+ and $\Gamma_6^+ + \Gamma_7^+$ induces a strong hybridization between the p orbitals of Sb atoms and the d orbitals of Rh atoms which is evidenced by the calculated negative $\xi = E_{\Gamma_6^+ + \Gamma_7^+} - E_{\Gamma_5^+}$ in Fig. 1(d). Correspondingly, in the highest valence band, the part far away from the Γ point is mainly contributed from the p orbitals of Sb atoms. However, the weight of Rh-4d orbitals [indicated by the radii of circles in the band line of Figs. 2(a) and 2(b)] increases when approaching the Fermi level and becomes dominant. This clearly indicates a band inversion between Rh-d and Sb-p orbitals. The highest valence band and the lowest conduction band form the irreducible representations $\Gamma_6^+ + \Gamma_7^+$, and the band Γ_5^- sits above all these bands. However, there is no influence on the double-degenerated bands $\Gamma_6^+ + \Gamma_7^+$ at Γ because the double degeneracy is enforced by the $m3$ double point group. Therefore the Fermi energy of $RhSb_3$ is pinned to the doublet $\Gamma_6^+ + \Gamma_7^+$ and is protected by symmorphic crystalline symmetry and time-reversal symmetry [47]. As shown in the band structure in Fig. 2(b), a

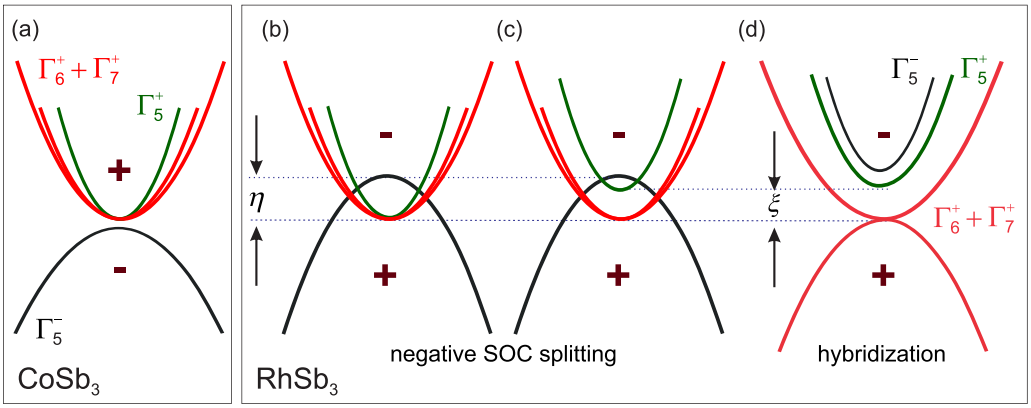

FIG. 1. Band inversion and symmetry-enforced Fermi degeneracy of unfilled skutterudite compound $RhSb_3$. (a) Schematic of band ordering in $CoSb_3$ close to the Fermi level, showing the valence band with an irreducible representation Γ_5^- and the conduction bands with irreducible representations Γ_5^+ and $\Gamma_6^+ + \Gamma_7^+$ touching at the Γ point. (b) The stronger SOC in Rh atoms of $RhSb_3$ pushes the band Γ_5^- up. The energy difference η between $\Gamma_6^+ + \Gamma_7^+$ and Γ_5^-, indicating the strength of the band inversion, becomes negative. (c) The SOC in $RhSb_3$ also lifts the degeneracy between Γ_5^+ and $\Gamma_6^+ + \Gamma_7^+$. (d) Finally, the overlap of the valence band Γ_5^- and the conduction bands Γ_5^+ and $\Gamma_6^+ + \Gamma_7^+$ induces a strong hybridization between the p orbitals of Sb atoms and the d orbitals of Rh atoms which is evidenced by the calculated negative energy difference ξ between $\Gamma_6^+ + \Gamma_7^+$ and Γ_5^+, giving the final band order of $RhSb_3$.

Dirac-like quasilinear dispersion persists over a wide energy range, with a more parabolic dispersion appearing in a very small energy window of ∼20 meV close to the Fermi level as shown in Fig. 2(b). The resultant calculated Fermi surface is an extremely small isotropic hole pocket centered at the Γ point [Fig. 2(c)]. Together, the band inversion and degeneracy near the Fermi level point to $RhSb_3$ as a type of ESFD. The ESFD is easily tuned to a topological insulator by symmetry breaking such as a uniaxial strain in the z direction. In other words, an infinitesimal symmetry breaking perturbation can lead it to a topological insulating phase, which is confirmed by the Fu-Kane Z_2 invariants ($\nu_0 = 1,\ \nu_1 = \nu_2 = \nu_3 = 0$) in the calculation with uniaxial strain (shown in Fig. S2 of the Supplemental Material).

To evaluate and confirm the nontrivial topology of these bands, we performed both ARPES and quantum oscillations experiments. Photon-energy-dependent ARPES measurements confirm the presence of a linearly dispersive three-dimensional hole pocket around Γ. The sample was cleaved to expose the (001) surface. Assuming a 10 eV inner potential, at 140 eV photon energy the momentum probed along the c axis corresponds to $k_z \sim 4.5 \times 2\pi/c$ ($\pi/c = \Gamma -$

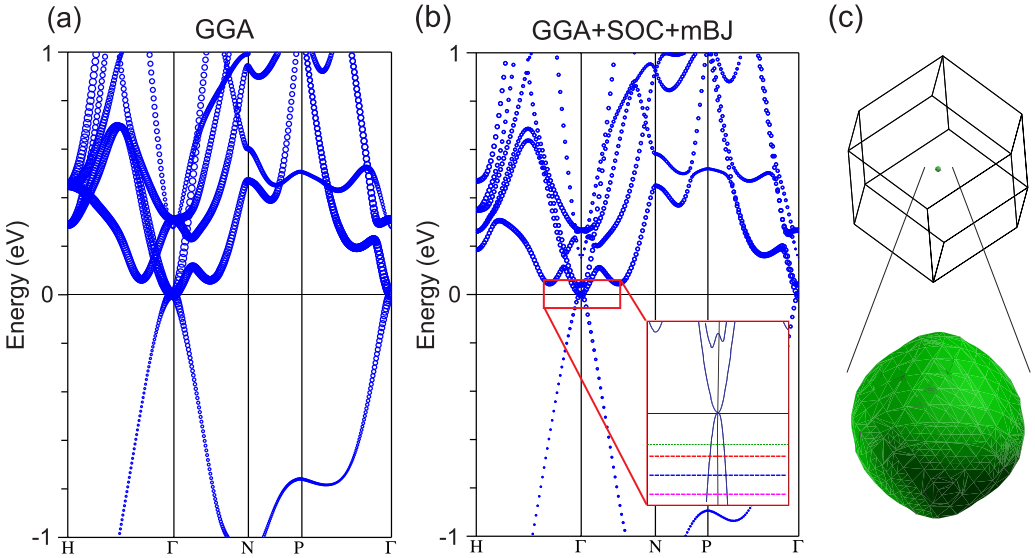

FIG. 2. Calculated electronic structure of $RhSb_3$. (a) and (b) The electronic structure of $RhSb_3$ was calculated from first principles using two methods: Without spin-orbit coupling using PBE potential (a) and with spin-orbit coupling and modified Becke-Johnson potential (b) (see text). The radii of circles denoting band lines are drawn proportional to the Rh-4d orbital weight. The inset in (b) is an enlarged part of the band structure around the Fermi level. The green, red, blue, and pink dashed lines indicate the positions of the Fermi levels for samples D, E, C, and A. (c) The calculated Fermi surface of $RhSb_3$ is represented in the first Brillouin zone and is extended below and enlarged by a factor of 50 for clarity.

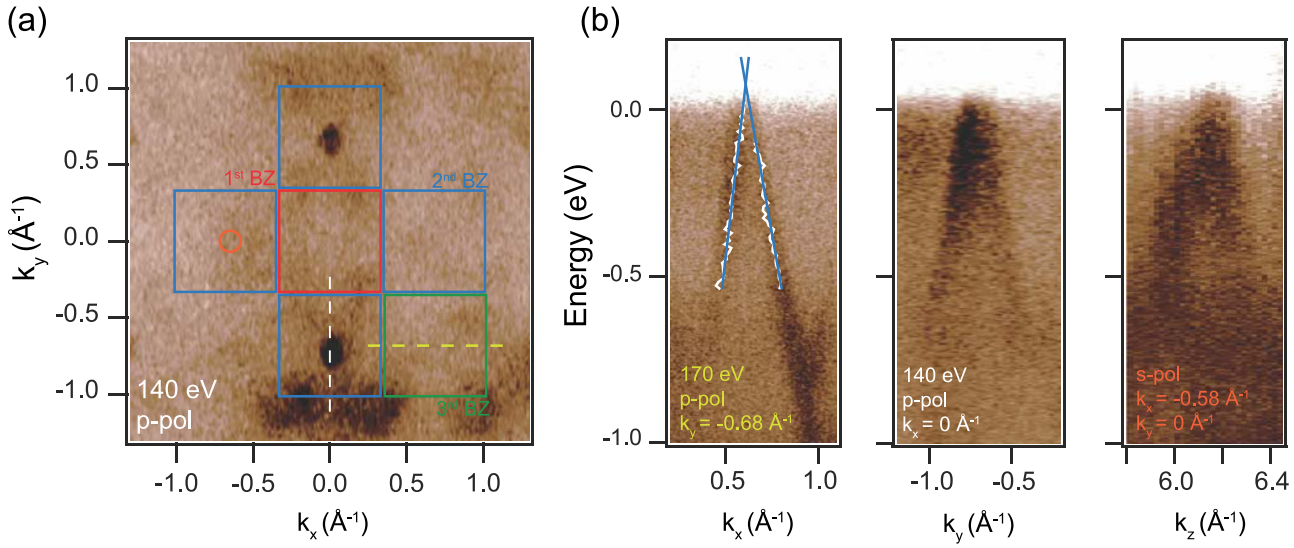

FIG. 3. Linear dispersion of $RhSb_3$ band structure from photon-energy-dependent ARPES at $T = 80$ K. (a) Fermi surface at 140 eV, p polarization (p-pol). The red square shows the first surface-projected Brillouin zone for the (100) surface, while the blue and green squares are the second and third zones (see more details in the Supplemental Material). (b) ARPES band mapping along the k_x, k_y, and k_z directions. Left panel: band mapping along the $k_y = -0.68$ Å^{-1} line in the third BZ [yellow dashed line in (a), 170 eV ($k_z \sim 5 \times 2\pi/c$), p polarization]. White solid curves show the peak position of the momentum distribution curves from a double-Gaussian fit, while blue solid lines are the result of a linear fit of the band dispersion. Central panel: band mapping along the $k_x = 0$ Å^{-1} line in the second BZ [white dashed line in (a), 140 eV ($k_z \sim 4.5 \times 2\pi/c$), p polarization]. Right panel: k_z dependence, assuming 10 eV inner potential, of the hole pocket in the second BZ at $(k_x, k_y) = (-0.57$ Å^{-1}, 0 Å$^{-1})$ [orange circle in (a), s polarization (s-pol)].

H). As a consequence of the body-centered-cubic structure, the Γ points from adjacent surface-projected BZs are characterized by a π/c offset in k_z. For this reason, holelike Fermi surface pockets can be observed in Fig. 3(a) only around the Γ points of the second BZ. Furthermore, due to matrix element effects, when using linear horizontal polarization (p), the second BZ hole pockets are detected only along the $k_x = 0$ Å^{-1} line while, with linear vertical polarization (s), those same pockets are observed exclusively along the $k_y = 0$ Å^{-1} line (see Fig. S3 of the Supplemental Material).

The resultant ARPES band mapping along k_x, k_y, and k_z directions is presented in Fig. 3(b). As a consequence of matrix element effects and to maximize the photoemission intensity from the hole pocket, these three cuts have been acquired in different regions of momentum space using different photon energies and incident polarizations. The left and central panels of Fig. 3(b) present the band mapping along the k_x and k_y directions [yellow and white dashed lines in Fig. 3(a), respectively]. By fitting the momentum distribution curves in the left panel, we estimate a Fermi velocity of $(0.6 \pm 0.2) \times 10^6$ m/s (4 ± 1.2 eV Å). In order to verify the three-dimensional nature of the detected pocket, photon-energy scans were performed to probe the k_z dependence. As shown in the right panel of Fig. 3(b), the photoemission intensity at $(k_x, k_y) = (-0.57$ Å^{-1}, 0 Å$^{-1})$ (slightly off the Γ point) changes as a function of energy, qualitatively defining a nearly isotropic three-dimensional-cone-like dispersion for the hole pocket. This is in good agreement with band structure calculations and, for comparison, is in contrast to observations of Cd_2As_3, where the Fermi velocity is markedly anisotropic [12]. Furthermore, the field angular dependence of the frequency of quantum oscillations in $RhSb_3$ crystal (shown in Fig. S4 of the Supplemental Material) exhibits very little variation with field angle orientation, confirming the case for a nearly spherical bulk three-dimensional Fermi pocket.

Magnetotransport and Shubnikov–de Haas (SdH) quantum oscillation experiments were performed on five representative samples (samples A to E). Magnetic fields applied along the principal axis in a transverse configuration significantly enhance the resistivity of $RhSb_3$ in all samples. The MR $[= (\rho_{xx}(B) - \rho_{xx}(0))/\rho_{xx}(0)]$ is linear in the high-field region, as evidenced by the field derivative of MR at different temperatures for sample D shown in Fig. 4(a) and in Fig. S8 of the Supplemental Material, and it does not show any sign of saturation up to a 64 T pulsed field but exhibits quantum oscillations above 10 T [also observed in the Hall resistivity, Fig. 4(b)]; it continues to increase above the quantum limit of ∼35 T. The MR ratio is close to the reported value ($\sim 10^3$–10^6) observed in both the Dirac material Cd_3As_2 and the TaAs family of Weyl materials [25,26,28,30–33]. As shown in Fig. 4(c), the MR has a strong temperature dependence, driving a semimetallic character in zero field toward a semiconductorlike behavior with a saturating resistivity at the lowest temperatures. While the absolute MR amplitude varies among different samples and is dependent on the residual resistivity ratio of the crystals as shown in Fig. 5 for samples A, B, C, and E, all crystals show a crossover from semimetallic character to semiconductorlike behavior driven by magnetic field (shown in Fig. S5 of the Supplemental Material).

Figure 4(b) presents the Hall resistivity ρ_{xy} of $RhSb_3$ as a function of field at different temperatures. In fields below 6 T, ρ_{xy} is linear and nearly temperature independent, while showing large quantum oscillations at higher fields that degrade with increasing temperature. It deviates slightly from

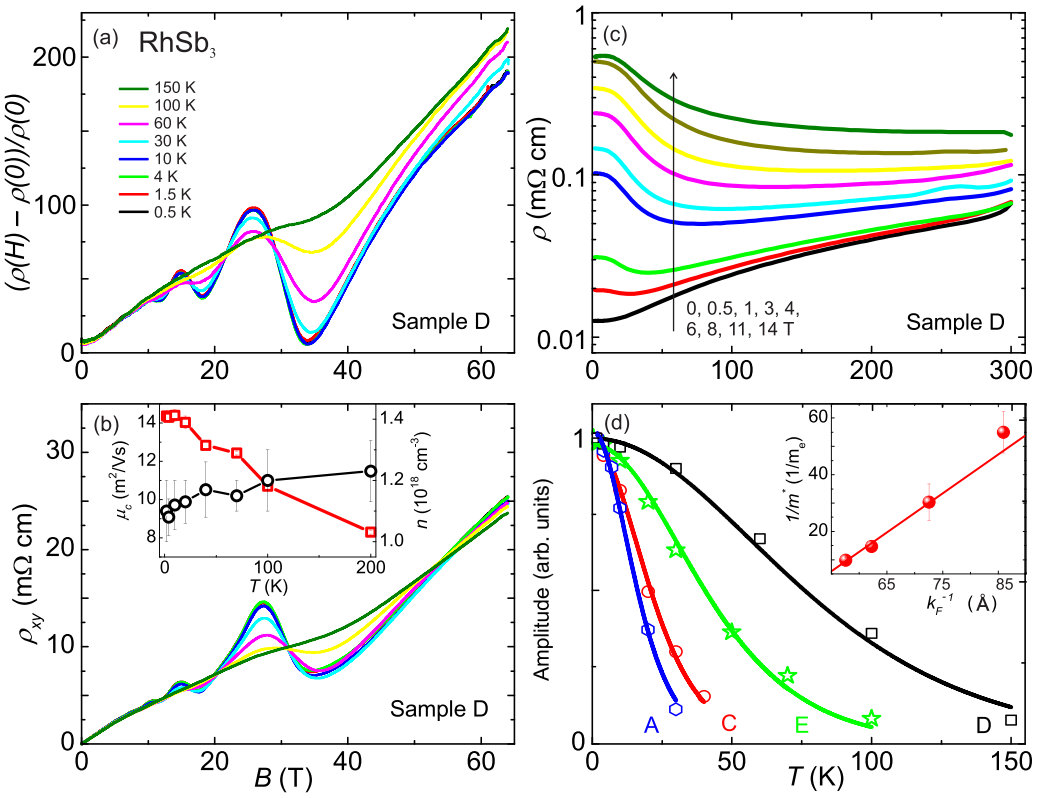

FIG. 4. Large magnetoresistance, high carrier mobility, and quantum oscillations of $RhSb_3$ single crystals. (a) Magnetoresistance of $RhSb_3$ sample D for field orientation transverse to current direction, showing very large nonsaturating enhancement up to 65 T pulsed field and prominent Shubnikov–de Haas oscillations up to temperatures of 150 K. (b) Hall resistivity ρ_{xy} of sample D [same temperature values as in (a)], with carrier mobility (red squares) and density (black circles) extracted from fitting of data shown in the inset. (c) Temperature dependence of the resistivity of sample D at different magnetic fields. (d) Amplitudes of Shubnikov–de Haas oscillations of the Fermi pocket as a function of temperature T, for four samples with varying carrier densities. The solid curves are fits to the Lifshitz-Kosevich formula for samples A, C, D, and E, which exhibit effective mass ratios m^*/m_e of 0.102(8), 0.066(7), 0.018(2), and 0.033(4), respectively, corresponding to oscillation frequencies of 71, 60, 33, and 43 T, respectively. The inset shows the linear relation of $\frac{1}{m^*}$ vs $k_F^{-1} = \sqrt{\frac{\pi}{F}}$ for these samples (spheres), revealing the Dirac-like dispersion (solid line fit) for $RhSb_3$.

the linear behavior at the higher magnetic field, possibly due to a shift in the chemical potential with the magnetic field as shown in Bi_2Se_3 [58]. The carrier density n of sample D is calculated by linear fits of the low-field ρ_{xy}, yielding a value $n \sim 1.1 \times 10^{18}$ cm^{-3} at low temperature and only ~10% variation upon increasing temperature as shown in the inset of Fig. 4(b). This is consistent with the zero-gap band structure depicted in Fig. 2. From the carrier density n and the zero-field resistivity $\rho_{xx} = 18$ μΩ cm, the classical mobility $\mu_c = 1/\rho_{xx}ne$ is calculated to approach 14 m^2/(V s) at 1.8 K, nearly those of graphene, Cd_3As_2, and TaAs/TaP, which fall in the range 1–100 m^2/(V s).

In addition to MR variations, SdH oscillation measurements performed on these different samples indicate a tunability of the oscillation frequency, and hence the carrier density and corresponding chemical potential variation, as shown in Fig. 6 for samples A, C, D, and E. Quantum oscillations in conductivity are given by

$$\Delta\sigma_{xx}(T, B) = A(T, B)\cos\{2\pi[(F/B) + \phi]\}, \quad (1)$$

with the nonoscillating amplitude $A(T, B) = e^{-2\pi^2 k_B T_D/\hbar\omega_c}\frac{2\pi^2 k_B T/\hbar\omega_c}{\sinh(2\pi^2 k_B T/\hbar\omega_c)}$, Dingle temperature T_D, cyclotron frequency $\omega_c = eB/m^*$ with effective mass m^*, phase factor $\phi = -1/2 + \beta + \delta$, and SdH frequency F of the oscillation corresponding to the cross section of the Fermi surface defined by the cyclotron orbits [59]. For a trivial parabolic dispersion, $\beta = 0$ and therefore the Berry's phase is zero, while $\beta = 1/2$ for a Dirac dispersion giving a Berry's phase of π. δ is a phase shift resulting from the curvature of the Fermi surface in the third direction, taking a value of $\delta = 0$ ($\pm\frac{1}{8}$) for a two-dimensional (three-dimensional) Fermi surface [60–63]. The frequency F is given by the Onsager relation $F = \frac{\hbar\pi k_F^2}{2\pi e}$ with k_F being the Fermi wave vector in the spherical Fermi surface approximation.

As evident in Figs. 4(a) and 4(b), the SdH oscillations of sample D have a very small frequency, which is 33 T as extracted from fast Fourier transform (FFT) analysis of the background-subtracted resistivity [Fig. 6(c)]. This value corresponds to wave vector $k_F = 0.04(5)$ Å^{-1} and a very small carrier density $n_{SdH} = 0.8(1) \times 10^{18}$ cm^{-3}, which is consistent with Hall resistivity results. The other three crystals also exhibit SdH oscillations (Figs. 5 and 6) with varying amplitudes and frequency. FFT analysis results in Fig. 6 yield a relatively large variation in frequencies: 71, 60, and 43 T for

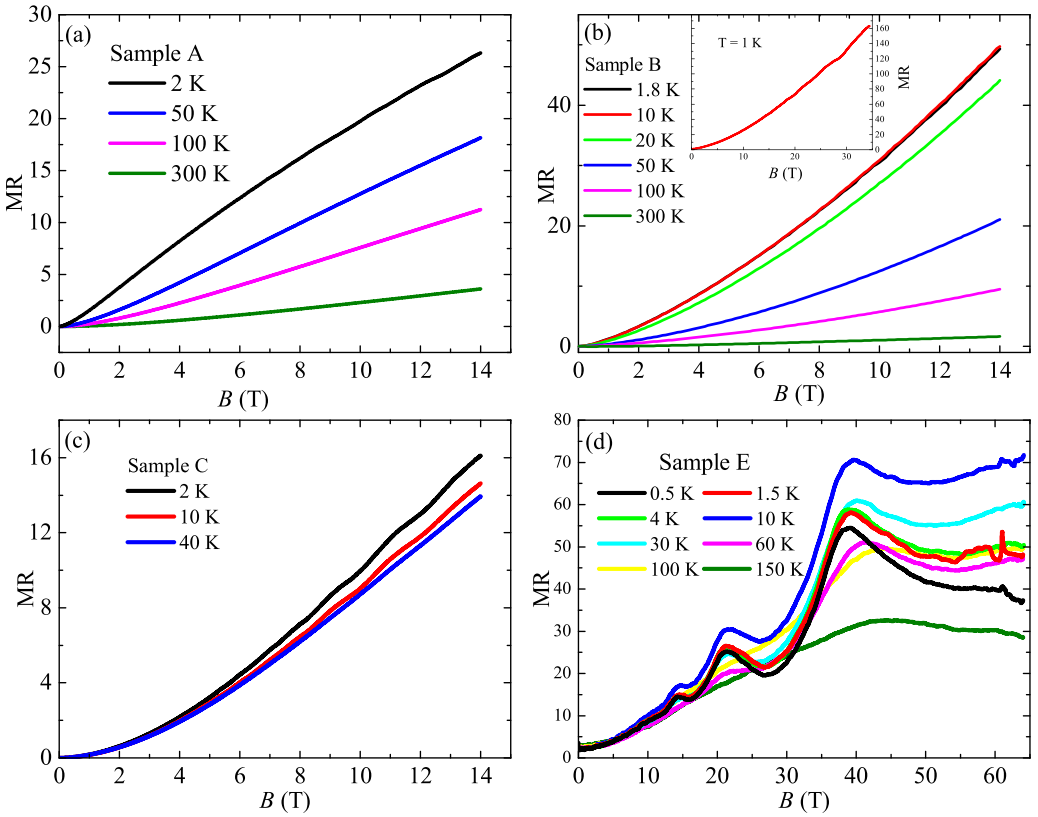

FIG. 5. Field dependence of the transverse magnetoresistance at different temperatures for four different $RhSb_3$ single crystals: sample A (a), sample B (b), sample C (c), and sample E (d). The inset in (b) shows the magnetoresistance of sample B in fields up to 35 T and 1 K. Samples A, C, and E show clear quantum oscillation beginning at ∼10 T.

samples A, C, and E, respectively. Interestingly, the amplitude of oscillations appears to be suppressed at different temperatures for each sample. While oscillations are still evident at 150 K for sample D (Fig. 4), they disappear near 30, 50, and 100 K for samples A, C, and E, respectively. This suggests that samples with smaller frequency (or carrier density) have charge carriers with systematically smaller effective masses. The decaying of the amplitude of SdH oscillation with temperature is described by the Lifshitz-Kosevich (LK) formula $A(T, B)$, which is the nonoscillating amplitude component of Eq. (1). As shown in Fig. 4(d), tracking the FFT amplitudes of all four samples as a function of temperature indeed shows a systematic trend. Fitting to the LK formula gives effective mass ratios m^*/m_e of 0.102(8), 0.066(7), 0.033(4), and 0.018(2) for samples A, C, E, and D, respectively, in descending mass order.

The effective mass in $RhSb_3$ is extremely light, being rivaled only by InSb, which has an effective mass $\sim 0.014m_e$ that yields observable oscillations up to 175 K [64,65]. The effective mass in $RhSb_3$ is also in fact comparable to those observed in typical Dirac ($0.023m_e$ in Cd_3As_2 [25,26]) and Weyl ($0.033m_e$ in NbAs [32], $0.076m_e$ in NbP [28], and $0.15m_e$ in TaAs [66]) semimetals. However, in $RhSb_3$ the systematic variation of m^* with F is indicative of a departure from the expectations for a parabolic dispersion. The effective mass, defined as $m^* = \hbar k_F/v_F$, should be constant for a parabolic band with different carrier densities since the Fermi velocity $v_F = \frac{1}{\hbar}\frac{\partial \varepsilon}{\partial k}|_{k_F} \propto k_F$ with ε being the band energy. However, this is not true for Dirac fermions with a linear dispersion, where v_F is a constant. For instance, in graphene it is expected that m^* is proportional to the square root of carrier density since $k_F = (\pi n_s)^{1/2}$, which was indeed confirmed by several experiments [67,68]. A similar phenomenon has also been shown in Cd_3As_2 [26]. In $RhSb_3$, the relation between m^* and k_F follows the equation above very well, as shown for all four samples in Fig. 4(d), except for an intercept which is possibly due to the breakdown of the semiclassical transport theory close to the quantum limit. This gives a constant $v_F = 1.3 \times 10^6$ m/s that is close to the ARPES value and also to that of Cd_3As_2 ($\sim 4 \times 10^6$ m/s) and NdP ($\sim 4.8 \times 10^5$ m/s).

The observation of a constant Fermi velocity with varying carrier concentration in $RhSb_3$ directly confirms that the bulk carriers have a linear dispersion very close to the degeneracy point, and the extreme values of m^* and v_F are considered to be responsible for the high mobility values. The topological nature of this band structure can be further explored by analysis of the phase factor of the quantum oscillations as indicated in Eq. (1). Experimentally, this phase shift in the semiclassical regime can be obtained from an analysis of the relation between the Landau level (LL) index N and energy, widely represented in a so-called fan diagram of integer N plotted as a function of inverse field $1/B$. The slope of such a plot is dependent on the oscillation frequency F, and the

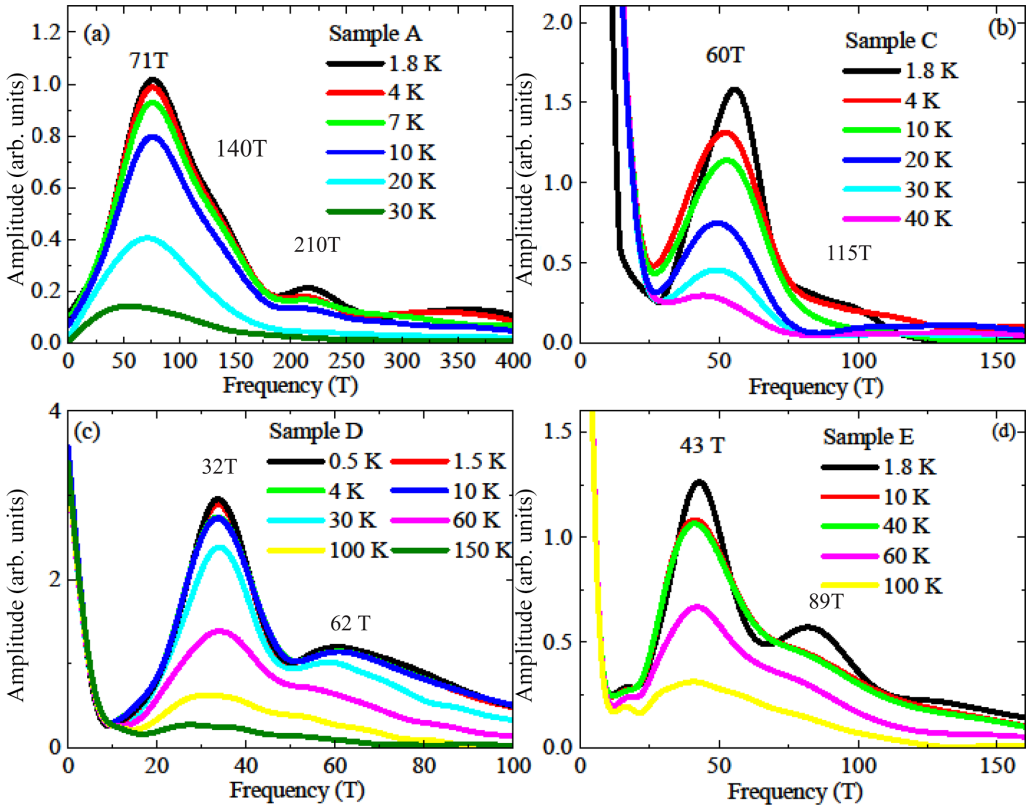

FIG. 6. The FFT spectra of Shubnikov–de Haas oscillations measured at different temperatures for sample A (a), sample C (b), sample D (c), and sample E (d).

y-axis intercept yields the Berry's phase β, in units of 2π. For a topologically trivial material with parabolic dispersion, an intercept of zero is expected, while that with a chiral Dirac dispersion would possess finite Berry curvature and therefore a Berry's phase of value π.

Figure 7(a) presents the oscillatory component of the conductivity $\Delta\sigma_{xx}$ of samples C, D, and E as a function of $1/B$. Assigning the minima and maxima of $\Delta\sigma_{xx}$ to integer (N) and half-integer ($N + 1/2$) indices (for the oscillation in the high-field part, the position of minima is defined as an average of two subminima due to the spin splitting), respectively, yields the LL fan diagram as shown in Fig. 7(b), demonstrating the variation in slopes that correspond to the different carrier densities of each sample. A linear extrapolation of N versus $1/B$ to the infinite-field limit for each sample yields finite intercepts of 0.352(4), 0.381(2), and 0.373(6) for samples C, D, and E, respectively. To properly extract the Berry's phase values, one must consider the phase shift due to geometry. Taking the $\delta = -\frac{1}{8}$ phase shift due to the spherical geometry of the Fermi surface (the hole pocket) of $RhSb_3$ into account, the measured intercept values are very close to the adjusted value 3/8 corresponding to the geometry-adjusted phase shift of $1/2 + \delta$, yielding a phase factor $\beta = \gamma + \frac{1}{8}$ for a Berry's phase of $0.92(1)\pi$, $1.02(1)\pi$, and $0.98(1)\pi$ for samples C, D, and E, respectively. Because the linear extrapolation of the LL indices is a simplistic fit of the LL spectrum, we have implemented a global fitting routine to further confirm the nontrivial Berry's phase in this paper. The Zeeman factor $R_s = \cos(\frac{\pi g m^*}{2m_0})$ needs to be incorporated to capture the observable splitting. Using Eq. (1), the Zeeman factor can be merged into $\cos\{2\pi[(F/B) + \phi]\}$, obtaining

$$\begin{aligned}\Delta\sigma_{xx}(T,B) &= A(T,B)\cos\left(\frac{\pi g m^*}{2m_0}\right)\cos\left[2\pi\left(\frac{F}{B}+\phi\right)\right]\\ &= A(T,B)\left\{\cos\left[2\pi\left(\frac{F}{B}+\phi+\delta\phi\right)\right]\right.\\ &\quad\left.+\cos\left[2\pi\left(\frac{F}{B}+\phi-\delta\phi\right)\right]\right\},\end{aligned} \tag{2}$$

where $\delta\phi = \frac{g m^*}{4m_0}$. We fit $\Delta\sigma_{xx}$ of samples C, D, and E using the BUMPS code (see Methods section) [49] with Eq. (2) to yield well-converging fits (shown in Figs. S7 and S8 of the Supplemental Material) to the experimental data as shown in Fig. 7(a). The Berry's phases extracted from this global fitting procedure are $0.87(1)\pi$, $0.96(1)\pi$, and $0.81(1)\pi$ for samples C, D, and E, respectively, consistent with the LL index extrapolations and therefore unequivocally implying the presence of a nontrivial topology and the existence of Dirac quasiparticles in the bulk of $RhSb_3$. First-principles calculations suggest a parabolic dispersion around the degeneracy point and linear dispersion in the valence band away from the degeneracy point. While the energy resolution is not enough in both experiment (ARPES) and theoretical calculation to resolve the exact nature of the dispersion at the degeneracy point (i.e., linear or quadratic), the lack of any observable

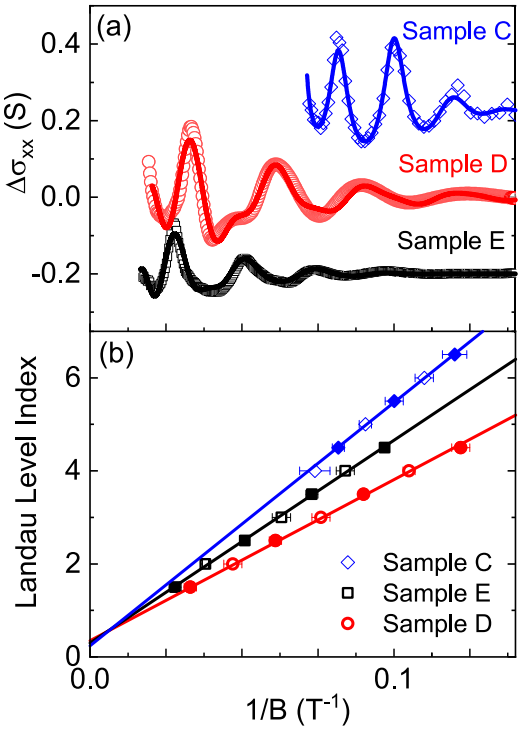

FIG. 7. Berry phase analysis of Shubnikov–de Haas oscillations in $RhSb_3$. (a) Quantum oscillations of background-subtracted conductivity $\Delta\sigma_{xx}$ as a function of inverse fields up to 64 T for samples D and E. The discrete symbols are the experimental data, while the curves are fits using a global fitting routine as described in the text. (b) Landau level (LL) index plot of oscillations of three samples, with integer levels assigned to the minima of $\Delta\sigma_{xx}$ and maxima assigned as half-integer indices. Solid lines are linear fits to the data, extrapolating to infinite-field intercepts that correspond to finite Berry's phase values of $0.92(1)\pi$, $1.02(1)\pi$, and $0.98(1)\pi$ for samples C, D, and E, respectively (see text).

curvature in the fan diagram, the observation of a constant Fermi velocity with varying carrier concentration, and the ARPES results suggest that the dispersion of the valence band in a range close to the chemical potentials of our crystals is very linear and Dirac-like [69], prompting further theoretical consideration of the exact nature of topology in this class of zero-gap topological semimetals.

IV. CONCLUSION

In summary, the electronic structure and transport properties of single crystals of the unfilled skutterudite material $RhSb_3$ were systematically studied by first-principles calculation, ARPES, and quantum oscillations measurements in magnetic fields up to 64 T. The electronic structure calculation indicates this material to be a zero-gap semimetal protected by symmetry with band inversion between Rh-4*d* and Sb-*p* orbitals. $RhSb_3$ single crystals exhibit unsaturated MR up to $(1.6 \times 10^4)\%$ in 35 T field at 0.4 K. Quantum oscillations are consistent with the presence of very small three-dimensional hole pockets with a nontrivial Berry phase shift, suggesting a nontrivial topological aspect to this system. The extremely light effective mass of carriers increases from $0.015(7)m_e$ to $0.102(8)m_e$ as a function of the carrier density or Fermi vector in different crystals. This and the ARPES results reveal that the Fermi level locates in the linear region of the valence band. Both the quantum oscillations and conventional Hall resistivity measurements reveal a very large mobility [$\sim 14\ m^2/(V\ s)$] which decreases with increasing temperature, while the carrier density shows very slight change. Our results postulate $RhSb_3$ as a zero-gap topological semimetal whose electronic structure and topological properties deserve further attention.

The open-source code VASP2TRACE and end-user button CHECKTOPOLOGICALMAT are available [70].

ACKNOWLEDGMENTS

The authors acknowledge useful discussions with A. Bernevig, Z. J. Wang, and J. Sau. This work was supported by the Gordon and Betty Moore Foundation's EPiQS Initiative through Grant No. GBMF9071. A portion of this work was performed at the National High Magnetic Field Laboratory, which is supported by National Science Foundation Cooperative Agreement No. DMR-1157490 and the State of Florida. This research was undertaken thanks in part to funding from the Max Planck–UBC Centre for Quantum Materials and the Canada First Research Excellence Fund, Quantum Materials and Future Technologies Program. The work at UBC was supported by the Killam, Alfred P. Sloan, and Natural Sciences and Engineering Research Council of Canada's (NSERC's) Steacie Memorial Fellowships (A.D.); the Alexander von Humboldt Fellowship (A.D.); the Canada Research Chairs Program (A.D.); and the NSERC, Canada Foundation for Innovation (CFI), and CIFAR Quantum Materials.

[1] M. Z. Hasan and C. L. Kane, Colloquium: Topological insulators, Rev. Mod. Phys. **82**, 3045 (2010).
[2] X.-L. Qi and S.-C. Zhang, Topological insulators and superconductors, Rev. Mod. Phys. **83**, 1057 (2011).
[3] S. M. Young, S. Zaheer, J. C. Y. Teo, C. L. Kane, E. J. Mele, and A. M. Rappe, Dirac Semimetal in Three Dimensions, Phys. Rev. Lett. **108**, 140405 (2012).
[4] X. Wan, A. M. Turner, A. Vishwanath, and S. Y. Savrasov, Topological semimetal and Fermi-arc surface states in the electronic structure of pyrochlore iridates, Phys. Rev. B **83**, 205101 (2011).
[5] C. Fang, M. J. Gilbert, X. Dai, and B. A. Bernevig, Multi-Weyl Topological Semimetals Stabilized by Point Group Symmetry, Phys. Rev. Lett. **108**, 266802 (2012).
[6] T. Bzdušek, Q. Wu, A. Rüegg, M. Sigrist, and A. A. Soluyanov, Nodal-chain metals, Nature (London) **538**, 75 (2016).
[7] A. A. Burkov, M. D. Hook, and L. Balents, Topological nodal semimetals, Phys. Rev. B **84**, 235126 (2011).
[8] Z. Wang, Y. Sun, X.-Q. Chen, C. Franchini, G. Xu, H. Weng, X. Dai, and Z. Fang, Dirac semimetal and topological phase transitions in A_3Bi (A = Na, K, Rb), Phys. Rev. B **85**, 195320 (2012).

[9] Z. Wang, H. Weng, Q. Wu, X. Dai, and Z. Fang, Three-dimensional Dirac semimetal and quantum transport in Cd_3As_2, Phys. Rev. B **88**, 125427 (2013).

[10] S. Borisenko, Q. Gibson, D. Evtushinsky, V. Zabolotnyy, B. Büchner, and R. J. Cava, Experimental Realization of a Three-Dimensional Dirac Semimetal, Phys. Rev. Lett. **113**, 027603 (2014).

[11] M. Neupane, S.-Y. Xu, R. Sankar, N. Alidoust, G. Bian, C. Liu, I. Belopolski, T.-R. Chang, H.-T. Jeng, H. Lin, A. Bansil, F. Chou, and M. Z. Hasan, Observation of a three-dimensional topological Dirac semimetal phase in high-mobility Cd_3As_2, Nat. Commun. **5**, 3786 (2014).

[12] Z. K. Liu, J. Jiang, B. Zhou, Z. J. Wang, Y. Zhang, H. M. Weng, D. Prabhakaran, S.-K. Mo, H. Peng, P. Dudin, T. Kim, M. Hoesch, Z. Fang, X. Dai, Z. X. Shen, D. L. Feng, Z. Hussain, and Y. L. Chen, A stable three-dimensional topological Dirac semimetal Cd_3As_2, Nat. Mater. **13**, 677 (2014).

[13] S. Jeon, B. B. Zhou, A. Gyenis, B. E. Feldman, I. Kimchi, A. C. Potter, Q. D. Gibson, R. J. Cava, A. Vishwanath, and A. Yazdani, Landau quantization and quasiparticle interference in the three-dimensional dirac semimetal Cd_3As_2, Nat. Mater. **13**, 851 (2014).

[14] B. Q. Lv, H. M. Weng, B. B. Fu, X. P. Wang, H. Miao, J. Ma, P. Richard, X. C. Huang, L. X. Zhao, G. F. Chen, Z. Fang, X. Dai, T. Qian, and H. Ding, Experimental Discovery of Weyl Semimetal TaAs, Phys. Rev. X **5**, 031013 (2015).

[15] S.-Y. Xu, I. Belopolski, N. Alidoust, M. Neupane, G. Bian, C. Zhang, R. Sankar, G. Chang, Z. Yuan, C.-C. Lee, S.-M. Huang, H. Zheng, J. Ma, D. S. Sanchez, B. Wang, A. Bansil, F. Chou, P. P. Shibayev, H. Lin, S. Jia *et al.*, Discovery of a Weyl fermion semimetal and topological Fermi arcs, Science **349**, 613 (2015).

[16] A. A. Soluyanov, D. Gresch, Z. Wang, Q. Wu, M. Troyer, X. Dai, and B. A. Bernevig, Type-II Weyl semimetals, Nature (London) **527**, 495 (2015).

[17] L. Huang, T. M. McCormick, M. Ochi, Z. Zhao, M.-T. Suzuki, R. Arita, Y. Wu, D. Mou, H. Cao, J. Yan, N. Trivedi, and A. Kaminski, Spectroscopic evidence for a type II Weyl semimetallic state in $MoTe_2$, Nat. Mater. **15**, 1155 (2016).

[18] A. Yamakage, Y. Yamakawa, Y. Tanaka, and Y. Okamoto, Line-node Dirac semimetal and topological insulating phase in noncentrosymmetric pnictides CaAgX (X = P, As), J. Phys. Soc. Jpn. **85**, 013708 (2016).

[19] L. M. Schoop, M. N. Ali, C. Straßer, A. Topp, A. Varykhalov, D. Marchenko, V. Duppel, S. S. P. Parkin, B. V. Lotsch, and C. R. Ast, Dirac cone protected by non-symmorphic symmetry and three-dimensional Dirac line node in ZrSiS, Nat. Commun. **7**, 11696 (2016).

[20] Z. Zhu, G. W. Winkler, Q. S. Wu, J. Li, and A. A. Soluyanov, Triple Point Topological Metals, Phys. Rev. X **6**, 031003 (2016).

[21] B. Bradlyn, L. Elcoro, J. Cano, M. G. Vergniory, Z. Wang, C. Felser, M. I. Aroyo, and B. A. Bernevig, Topological quantum chemistry, Nature (London) **547**, 298 (2017).

[22] B. Bradlyn, J. Cano, Z. Wang, M. G. Vergniory, C. Felser, R. J. Cava, and B. A. Bernevig, Beyond Dirac and Weyl fermions: Unconventional quasiparticles in conventional crystals, Science **353**, aaf5037 (2016).

[23] M. G. Vergniory, L. Elcoro, C. Felser, N. Regnault, B. A. Bernevig, and Z. Wang, A complete catalogue of high-quality topological materials, Nature (London) **566**, 480 (2019).

[24] Topological Materials Database, https://topologicalquantumchemistry.org/#/.

[25] T. Liang, Q. Gibson, M. N. Ali, M. Liu, R. J. Cava, and N. P. Ong, Ultrahigh mobility and giant magnetoresistance in the Dirac semimetal Cd_3As_2, Nat. Mater. **14**, 280 (2015).

[26] A. Narayanan, M. D. Watson, S. F. Blake, N. Bruyant, L. Drigo, Y. L. Chen, D. Prabhakaran, B. Yan, C. Felser, T. Kong, P. C. Canfield, and A. I. Coldea, Linear Magnetoresistance Caused by Mobility Fluctuations in n-Doped Cd_3As_2, Phys. Rev. Lett. **114**, 117201 (2015).

[27] Z. Wang and S.-C. Zhang, Chiral anomaly, charge density waves, and axion strings from Weyl semimetals, Phys. Rev. B **87**, 161107(R) (2013).

[28] C. Shekhar, A. K. Nayak, Y. Sun, M. Schmidt, M. Nicklas, I. Leermakers, U. Zeitler, Y. Skourski, J. Wosnitza, Z. Liu, Y. Chen, W. Schnelle, H. Borrmann, Y. Grin, C. Felser, and B. Yan, Extremely large magnetoresistance and ultrahigh mobility in the topological Weyl semimetal candidate NbP, Nat. Phys. **11**, 645 (2015).

[29] Q. Li, D. E. Kharzeev, C. Zhang, Y. Huang, I. Pletikosić, A. V. Fedorov, R. D. Zhong, J. A. Schneeloch, G. D. Gu, and T. Valla, Chiral magnetic effect in ZrTe5, Nat. Phys. **12**, 550 (2016).

[30] C.-L. Zhang, Z. Yuan, Q.-D. Jiang, B. Tong, C. Zhang, X. C. Xie, and S. Jia, Electron scattering in tantalum monoarsenide, Phys. Rev. B **95**, 085202 (2017)..

[31] X. Huang, L. Zhao, Y. Long, P. Wang, D. Chen, Z. Yang, H. Liang, M. Xue, H. Weng, Z. Fang, X. Dai, and G. Chen, Observation of the Chiral-Anomaly-Induced Negative Magnetoresistance in 3D Weyl Semimetal TaAs, Phys. Rev. X **5**, 031023 (2015).

[32] Y. Luo, N. J. Ghimire, M. Wartenbe, H. Choi, M. Neupane, R. D. McDonald, E. D. Bauer, J. Zhu, J. D. Thompson, and F. Ronning, Electron-hole compensation effect between topologically trivial electrons and nontrivial holes in NbAs, Phys. Rev. B **92**, 205134 (2015).

[33] M. N. Ali, L. M. Schoop, C. Garg, J. M. Lippmann, E. Lara, B. Lotsch, and S. S. P. Parkin, Butterfly magnetoresistance, quasi-2D Dirac Fermi surface and topological phase transition in ZrSiS, Sci. Adv. **2**, e1601742 (2016).

[34] F. F. Tafti, Q. D. Gibson, S. K. Kushwaha, N. Haldolaarachchige, and R. J. Cava, Resistivity plateau and extreme magnetoresistance in LaSb, Nat. Phys. **12**, 272 (2016).

[35] K. Wang, D. Graf, L. Li, L. Wang, and C. Petrovic, Anisotropic giant magnetoresistance in $NbSb_2$, Sci. Rep. **4**, 7328 (2014).

[36] B. Shen, X. Deng, G. Kotliar, and N. Ni, Fermi surface topology and negative longitudinal magnetoresistance observed in the semimetal $NbAs_2$, Phys. Rev. B **93**, 195119 (2016).

[37] Y. Luo, R. D. McDonald, P. F. S. Rosa, B. Scott, N. Wakeham, N. J. Ghimire, E. D. Bauer, J. D. Thompson, and F. Ronning, Anomalous electronic structure and magnetoresistance in $TaAs_2$, Sci. Rep. **6**, 27294 (2016).

[38] J. Nayak, S.-C. Wu, N. Kumar, C. Shekhar, S. Singh, J. Fink, E. E. D. Rienks, G. H. Fecher, S. S. P. Parkin, B. Yan, and C. Felser, Multiple Dirac cones at the surface of the topological metal LaBi, Nat. Commun. **8**, 13942 (2017).

[39] Y. Wu, T. Kong, L.-L. Wang, D. D. Johnson, D. Mou, L. Huang, B. Schrunk, S. L. Bud'ko, P. C. Canfield, and A. Kaminski, Asymmetric mass acquisition in LaBi: Topological semimetal candidate, Phys. Rev. B **94**, 081108(R) (2016).

[40] R. Lou, B.-B. Fu, Q. N. Xu, P.-J. Guo, L.-Y. Kong, L.-K. Zeng, J.-Z. Ma, P. Richard, C. Fang, Y.-B. Huang, S.-S. Sun, Q. Wang, L. Wang, Y.-G. Shi, H. C. Lei, K. Liu, H. M. Weng, T. Qian, H. Ding, and S.-C. Wang, Evidence of topological insulator state in the semimetal LaBi, Phys. Rev. B **95**, 115140 (2017).

[41] L.-K. Zeng, R. Lou, D.-S. Wu, Q. N. Xu, P.-J. Guo, L.-Y. Kong, Y.-G. Zhong, J.-Z. Ma, B.-B. Fu, P. Richard, P. Wang, G. Liu, L. Lu, Y.-B. Huang, C. Fang, S.-S. Sun, Q. Wang, L. Wang, Y.-G. Shi, H. Weng *et al.*, Compensated Semimetal LaSb with Unsaturated Magnetoresistance, Phys. Rev. Lett. **117**, 127204 (2016).

[42] C. Xu, J. Chen, G.-X. Zhi, Y. Li, J. Dai, and C. Cao, Electronic structures of transition metal dipnictides XPn_2 (X = Ta, Nb; Pn = P, As, Sb), Phys. Rev. B **93**, 195106 (2016).

[43] D. Gresch, Q. Wu, G. W. Winkler, and A. A. Soluyanov, Hidden Weyl points in centrosymmetric paramagnetic metals, New J. Phys. **19**, 035001 (2017).

[44] D. J. Singh and W. E. Pickett, Skutterudite antimonides: Quasilinear bands and unusual transport, Phys. Rev. B **50**, 11235 (1994).

[45] J. C. Smith, S. Banerjee, V. Pardo, and W. E. Pickett, Dirac Point Degenerate with Massive Bands at a Topological Quantum Critical Point, Phys. Rev. Lett. **106**, 056401 (2011).

[46] Y. Tang, Z. M. Gibbs, L. A. Agapito, G. Li, H.-S. Kim, M. B. Nardelli, S. Curtarolo, and G. J. Snyder, Convergence of multi-valley bands as the electronic origin of high thermoelectric performance in $CoSb_3$ skutterudites, Nat. Mater. **14**, 1223 (2015).

[47] V. Pardo, J. C. Smith, and W. E. Pickett, Linear bands, zero-momentum Weyl semimetal, and topological transition in skutterudite-structure pnictides, Phys. Rev. B **85**, 214531 (2012).

[48] M. Yang and W.-M. Liu, The d-p band-inversion topological insulator in bismuth-based skutterudites, Sci. Rep. **4**, 5131 (2014).

[49] P. A. Kienzle, J. Krycka, N. Patel, and I. Sahin, Bumps: Curve fitting and uncertainty analysis (version 0.7.6), University of Maryland, College Park,2018.

[50] M. Weinert, E. Wimmer, and A. J. Freeman, Total-energy all-electron density functional method for bulk solids and surfaces, Phys. Rev. B **26**, 4571 (1982).

[51] P. Blaha, K. Schwarz, G. K. H. Madsen, D. Kvasnicka, and J. Luitz, *WIEN2k: An Augmented PlaneWave + Local Orbitals Program for Calculating Crystal Properties* (Technische Universität Wien, Austria, 2001).

[52] J. P. Perdew, K. Burke, and M. Ernzerhof, Generalized Gradient Approximation Made Simple, Phys. Rev. Lett. **77**, 3865 (1996).

[53] F. Tran and P. Blaha, Accurate Band Gaps of Semiconductors and Insulators with a Semilocal Exchange-Correlation Potential, Phys. Rev. Lett. **102**, 226401 (2009).

[54] J. Cano, B. Bradlyn, Z. Wang, L. Elcoro, M. G. Vergniory, C. Felser, M. I. Aroyo, and B. A. Bernevig, Building blocks of topological quantum chemistry: Elementary band representations, Phys. Rev. B **97**, 035139 (2018).

[55] Bilbao Crystallographic Server, https://www.cryst.ehu.es/cgi-bin/cryst/programs/bandrep.pl.

[56] See Supplemental Material at http://link.aps.org/supplemental/10.1103/PhysRevMaterials.7.074205 for supporting figures and data as described in the main text.

[57] K. Koga, K. Akai, K. Oshiro, and M. Matsuura, Electronic structure and optical properties of binary skutterudite antimonides, Phys. Rev. B **71**, 155119 (2005).

[58] B. Fauqué, N. P. Butch, P. Syers, J. Paglione, S. Wiedmann, A. Collaudin, B. Grena, U. Zeitler, and K. Behnia, Magnetothermoelectric properties of Bi_2Se_3, Phys. Rev. B **87**, 035133 (2013).

[59] D. Shoenberg, *Magnetic Oscillations in Metals* (Cambridge University Press, Cambridge, 1984).

[60] H. Murakawa, M. S. Bahramy, M. Tokunaga, Y. Kohama, C. Bell, Y. Kaneko, N. Nagaosa, H. Y. Hwang, and Y. Tokura, Detection of Berry's phase in a bulk Rashba semiconductor, Science **342**, 1490 (2013).

[61] L. P. He, X. C. Hong, J. K. Dong, J. Pan, Z. Zhang, J. Zhang, and S. Y. Li, Quantum Transport Evidence for the Three-Dimensional Dirac Semimetal Phase $InCd_3As_2$, Phys. Rev. Lett. **113**, 246402 (2014).

[62] I. A. Luk'yanchuk and Y. Kopelevich, Dirac and Normal Fermions in Graphite and Graphene: Implications of the Quantum Hall Effect, Phys. Rev. Lett. **97**, 256801 (2006).

[63] I. A. Luk'yanchuk and Y. Kopelevich, Phase Analysis of Quantum Oscillations in Graphite, Phys. Rev. Lett. **93**, 166402 (2004).

[64] J. Hu and T. F. Rosenbaum, Classical and quantum routes to linear magnetoresistance, Nat. Mater. **7**, 697 (2008).

[65] Y.-S. Kim, K. Hummer, and G. Kresse, Accurate band structures and effective masses for InP, InAs, and InSb using hybrid functionals, Phys. Rev. B **80**, 035203 (2009).

[66] S.-M. Huang, S.-Y. Xu, I. Belopolski, C.-C. Lee, G. Chang, B. Wang, N. Alidoust, G. Bian, M. Neupane, C. Zhang, S. Jia, A. Bansil, H. Lin, and M. Z. Hasan, A Weyl fermion semimetal with surface Fermi arcs in the transition metal monopnictide TaAs class, Nat. Commun. **6**, 7373 (2015).

[67] A. H. Castro Neto, F. Guinea, N. M. R. Peres, K. S. Novoselov, and A. K. Geim, The electronic properties of graphene, Rev. Mod. Phys. **81**, 109 (2009).

[68] K. S. Novoselov, A. K. Geim, S. V. Morozov, D. Jiang, M. I. Katsnelson, I. V. Grigorieva, S. V. Dubonos, and A. A. Firsov, Two-dimensional gas of massless Dirac fermions in graphene, Nature (London) **438**, 197 (2005).

[69] A. A. Taskin and Y. Ando, Berry phase of nonideal Dirac fermions in topological insulators, Phys. Rev. B **84**, 035301 (2011).

[70] https://www.cryst.ehu.es/cgi-bin/cryst/programs/magnetictopo.pl?tipog=gesp.